Chapter 2

Experimental techniques: Materials synthesis, Onboard Instrumentation, and Data analyzing tools

In this chapter, we provide a concise overview of the methodologies employed for sample preparation, along with the onboard instrumentations used for crystal structure analysis, thermal analysis, and microstructural studies. We also discuss data calibration tools such as X-ray Rietveld refinement, electrochemical study, and impedance spectroscopy. In the end, we describe the kinetics of electrochemical reactions with the help of Trassati and Dunn's methods

2.1 Overview

This chapter provides a detailed description of sample preparation, characterization techniques, and their underlying working principles. It is divided into three sections:

(1) The first section explores various materials-synthesis techniques.

(2) The second section discusses the various characterization tools utilized for crystal structure analysis and the electrochemical properties of the synthesized materials.

(3) The third section covers the kinetics of electrochemical reactions with the help of the Trassati and Dunn methods.

2.2 Synthesis Techniques

The synthesis of materials in the nano-regime can be classified into two categories: top-down and bottom-up approaches. The top-down approach involves reducing bulk materials into nano-dimensions using methods like ball milling and sputtering etc. On the other hand, the bottom-up approach entails constructing nanomaterials by assembling atoms or molecules one by one. Further, the morphology of the material is crucial in determining the electrochemical property of the material for supercapacitor applications. Selecting the right methodology is essential for creating superior electrodes. Different synthetic methods, such as the sol-gel route [127], hydrothermal approach [128], microwave-irradiation method [129], co-precipitation technique [130], Chemical-flux method [131], and solid-state ceramic route [132] can be employed for the formation of transition metal-based layered structure. Each method has its own advantages and disadvantages. Some of them are discussed as followings:

2.2.1 Co-precipitation method

The co-precipitation method is a chemical technique that allows for precise control over the chemical uniformity due to the molecular level of mixing of reactants at a low synthesis temperature [130]. This method is not only cost-effective but also provides control of various synthesis parameters, like the pH of the reaction mixture, the reaction temperature, etc. The co-precipitation process involves multiple steps such as mixing a solution of metal salts, precipitation, filtration, washing, drying, and finally calcination. The precipitation step

can be divided into three main components: nucleation, crystal growth, and aggregation of the primary precipitated particles. While nucleation and crystal growth often occur simultaneously, they can also be carried out independently. Larger clusters exceeding the critical size tend to continue growing, whereas smaller clusters tend to re-dissolve in the reaction mixture.

In the present work, $AgFeO_2$ nanoparticles were synthesized using a co-precipitation route. Typically, 5 mM of silver nitrate ($AgNO_3$, 99.9%, HIMEDIA) and 5 mM of iron nitrate ($Fe(NO_3)_3.9H_2O$, 98%, Merk) were dissolved in 200 ml of double distilled water with continuous stirring to make a homogeneous solution. To carry out complete precipitation, 50 ml of 5 M NaOH solution was gradually added drop by drop into the above solution, and the pH was adjusted to 9 by adding 5 ml of 25% ammonia solution. The resulting suspension was allowed to settle for 6 hours. Afterward, it was washed multiple times with double distilled water and ethanol. The filtrate was then collected and dried at 80°C for 12 hours in a vacuum oven. Subsequently, the dried material was calcined at 200, 400, and 550°C for 5 hours in an air atmosphere. The different samples obtained from the calcination process were denoted as AFO-80 (no calcination), AFO-200, AFO-400, and AFO-550, respectively. The synthesized powder samples had a deep brown color.

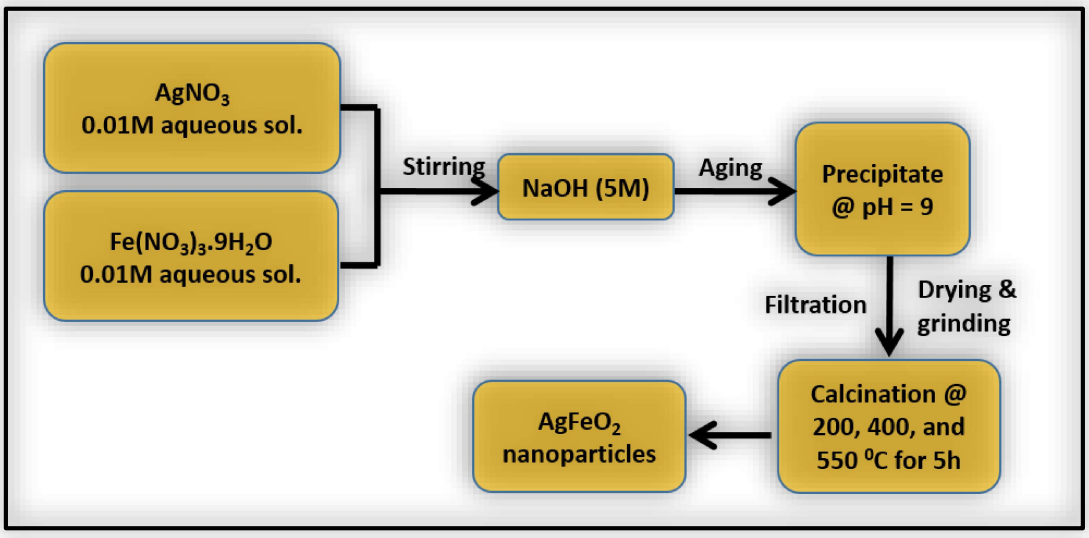

Figure 2.1: schematic diagram of the co-precipitation synthesis of $AgFeO_2$ nanoparticles

2.2.2 Chemical-flux method

Chemical flux method synthesis, also known as flux-growth method, is a versatile technique that allows the growth of single crystals with controlled sizes and shapes of various compounds, particularly inorganic compounds. The process involves the controlled dissolution of reactants in a flux medium at elevated temperatures which leads to the crystallization of the desired material as single crystals [131]. The temperature of the reaction mixture was set just above the melting point of the fluxing agent but below the decomposition temperature of the desired compound. It is particularly useful for compounds with high melting points or those that decompose at high temperatures. In the present work, crystallites of layered potassium manganese oxide, $K_{0.4}MnO_2.xH_2O$, were successfully grown using the chemical flux method. KNO_3 (Qualigenes, 98%) and Mn_2O_3 (Sigma-Aldrich, 99%) were used as precursor compounds, here, KNO_3 also served as a fluxing agent. The starting materials, KNO_3 (12.3 g) and Mn_2O_3 (2.0 g) were mixed in the molar ratio of K: Mn to 1:5 using mortar and pestle and kept in a platinum crucible. The mixed compound was heated at 700 °C for 24 h and was gradually cooled to 300 °C at a rate of 10 K/h followed by natural cooling to room temperature. The crucible was covered with a lid during the entire heat treatment. The sample was recovered by washing it several times with double distilled water and dried overnight at 80 °C. The prepared material was black in color.

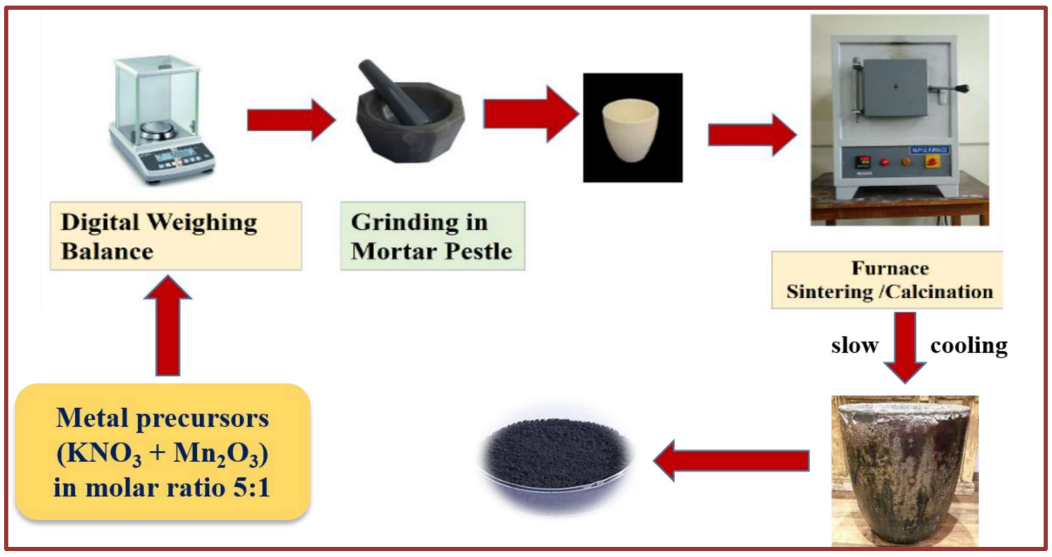

Figure 2.2: Schematic growth of the $K_{0.4}MnO_2.xH_2O$ crystallites.

2.2.3 Solid-state ceramic route

Solid-state synthesis, also known as mechanochemistry, is a powerful method used to fabricate materials without the involvement of liquid-phase reactions. It has gained significant attention in recent years due to its ability to produce more thermodynamically stable products with enhanced properties, including improved purity, homogeneity, and control over crystal structure [132]. Solid-state synthesis typically involves mixing of solid reactants with the help of mechanical forces, such as milling or grinding, either in the presence or absence of a catalyst or additive. These mechanical forces promote the mixing of reactants at the atomic level, enhance diffusion, and induce chemical reactions by breaking down the crystal lattice. One of the key advantages of solid-state synthesis is solvent-free processing, control over crystal structure, and the ability to produce complex materials, which can tune the properties of the resulting material.

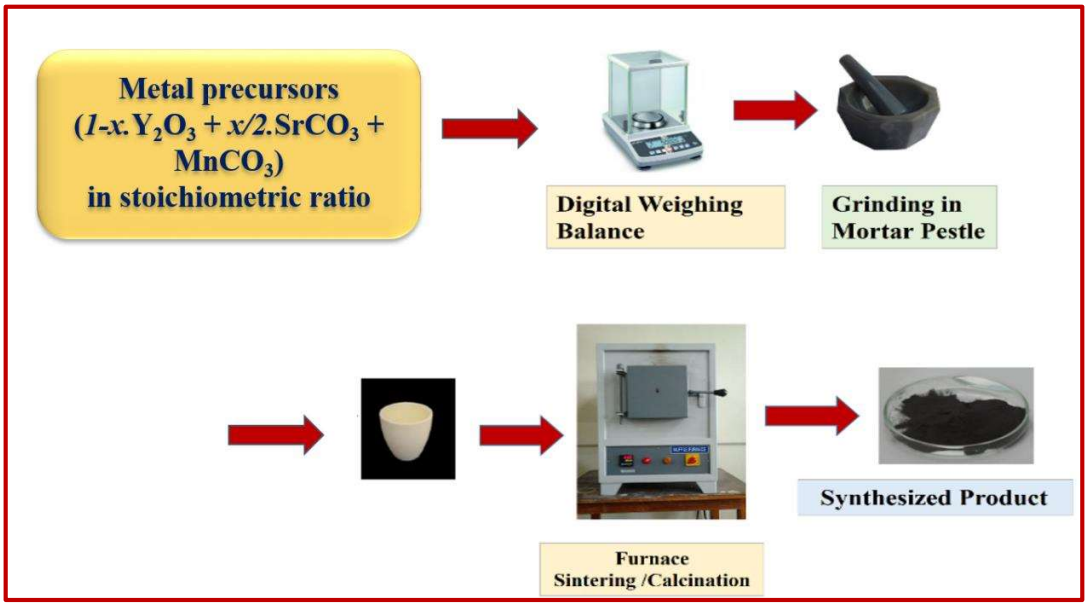

Figure 2.3: Flow chart of the solid-state synthesis of various Sr-doped $Y_{1-x}Sr_xMnO_3$

In the present work, the solid-state ceramic synthesis route was adopted to obtain crystalline Sr-doped $Y_{1-x}Sr_xMnO_3$ (x = 0, 0.2, 0.5, 0.7, 1.0). Y_2O_3 (99.9%), $SrCO_3$ (99.9%), and $MnCO_3$ (99.9%) were taken in a stoichiometric ratio and mixed in an agate mortar pestle for about 60 min. The mixture was first fired at 600 °C and then calcined at 1000 °C for 12 h in an alumina crucible for the preparation of $YMnO_3$ and $Y_{1-x}Sr_xMnO_3$ (x = 0.2, 0.5, 0.7,

1.0) followed by slow cooling to room temperature to get phase pure materials. The samples were denoted as YSMO-0, YSMO-20, YSMO-50, YSMO-70, and YSMO-100 for 0, 20, 50, 70, and 100% Sr doped $YMnO_3$, respectively.

2.2.4 Hydrothermal synthesis

In hydrothermal synthesis, different types of nanoparticles have been formed in a controlled environment. It involves the use of high temperature and pressure conditions to facilitate the formation of nanoscale materials in an aqueous solution. In hydrothermal synthesis, precursor solution containing metal ions are sealed in a high-pressure reaction vessel, such as a Teflon-lined autoclave, and subjected to elevated temperatures ranging from 100 to 300 °C. The high pressure within the reaction vessel helps to maintain the solution in a liquid state at temperatures above its boiling point, enabling the hydrothermal reaction to take place. The growth mechanism of nanoparticles in a hydrothermal synthesis process can be influenced by various factors, such as reaction temperature, pressure, precursor concentration, reaction time, and pH of the solution [128]. By adjusting these parameters, one can tailor the size, shape, and composition of the nanoparticles. Once the reaction time has been completed, the reaction vessel is allowed to cool down at room temperature, and the resulting nanoparticle suspension is recovered by centrifugation or filtration, followed by washing and drying steps to obtain a solid nanoparticle product. In the present work different Mn-based layered compounds ((γ-MnOOH, $LiMnO_2$-Li_2MnO_3, and spinel $LiMn_2O_4$)) were synthesized via two-step hydrothermal method.

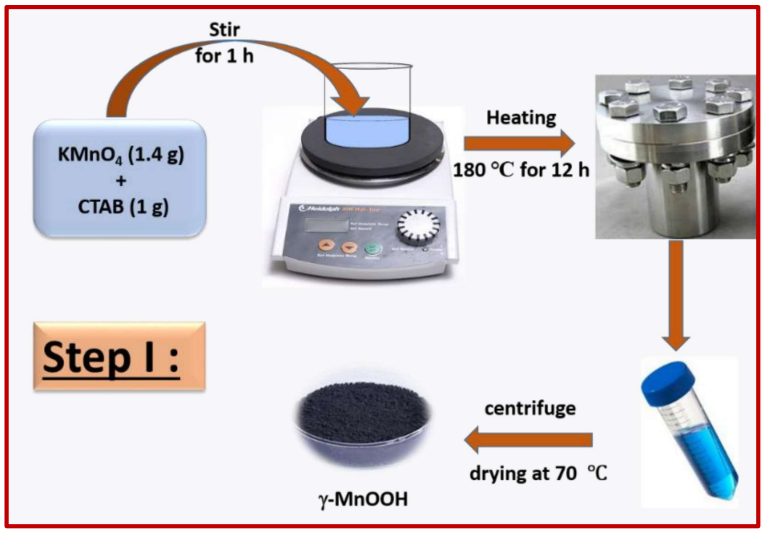

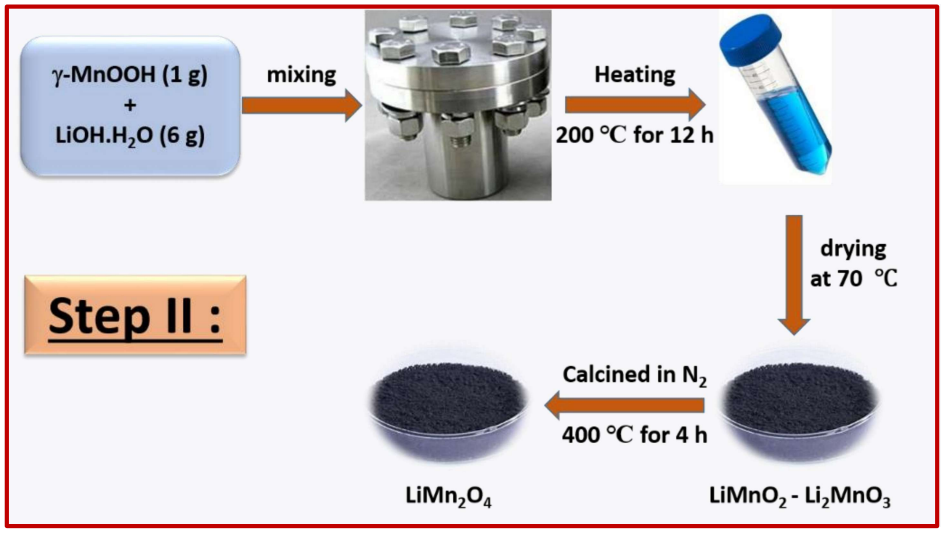

Figure 2.4: Two-step hydrothermal synthesis of different Mn-based layered compounds (γ-MnOOH, $LiMnO_2$-Li_2MnO_3, and spinel $LiMn_2O_4$)

2.3 Material characterization Techniques

This section outlines the characterization techniques employed in this study. The fundamentals of each method are briefly discussed in the next section. The primary techniques used are as follows:

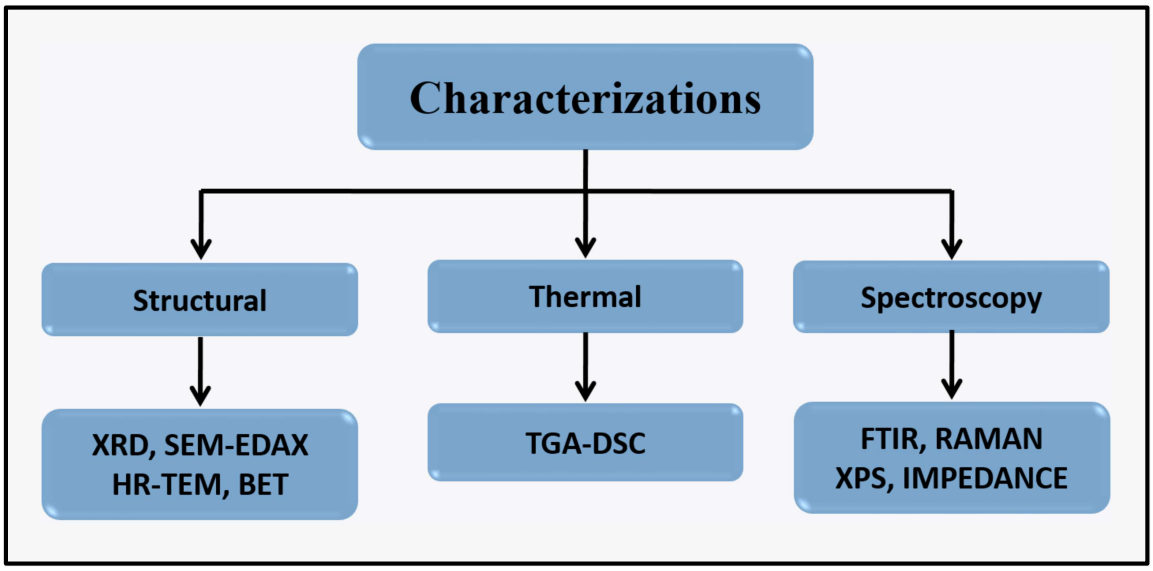

Figure 2.5: Different characterization techniques used for the sample analysis.

2.3.1 Powder X-ray Diffraction (XRD)

X-ray diffraction (XRD) is a widely used technique for characterizing materials without causing damage. It enables the determination of a material's phase, purity, and crystal structure. This technique relies on Bragg's law of diffraction, which was proposed by W. H. Bragg and his son W. L. Bragg. According to Bragg's law, when a monochromatic beam of X-rays strikes a set of evenly spaced crystal planes, the constructive interference of the diffracted X-rays only occurs under two conditions. First, the angle of incidence of the X-rays must be equal to the diffraction angle. Second, the difference in path length between the incident and diffracted X-rays must be an integral multiple of the X-ray wavelength. Mathematically, Bragg's law can be expressed as:

$$2d \sin\theta = n\lambda$$

where, λ is the wavelength of the X-ray, d is the inter planer spacing, θ is the angle of incidence, and n represents the order of diffraction.

Fig. 2.6 displays a schematic diagram that illustrates Bragg's law. Strong Bragg peaks occur at specific scattering angles when the constructive interference satisfies Bragg's law. The number of Bragg peaks in a diffraction pattern generally relies on the crystal symmetry of the material. Materials with low crystal symmetry, such as monoclinic, exhibit numerous Bragg peaks due to large number of lattice planes. On the other hand, materials with high crystal symmetry, such as cubic and tetragonal, have fewer Bragg peaks due to their limited number of lattice planes. In addition to crystal symmetry, the size, and shape of particles also affects the Bragg peaks.

A typical X-ray diffractometer consists of three essential parts: an X-ray generator, a sample holder, and a detector. In the X-ray generator, the cathode tube's filament is heated to generate electrons, which are then accelerated by applying high voltage. These accelerated electrons are directed toward a target material, causing it to be bombarded and produce characteristic X-rays. Copper (Cu) is the most commonly used target metal, generating characteristic X-rays with a wavelength of 1.5481 Å (angstroms). The characteristic X-rays are carefully focused and directed onto the sample holder, which holds the sample. The diffracted X-rays from the sample are captured by surrounding X-ray detectors, which

convert the X-ray signals into a count rate. Most x-ray diffractometers utilize the Bragg-Brentano parafocusing geometry, which provides a highly intense x-ray beam and excellent resolution. This geometry requires the sample to have a flat surface to ensure efficient collection of x-ray signals by the detector. In this setup, the incidence angle between the x-ray beam and the sample surface is always half of the detector angle. The sample and detector rotate at angles of θ/min and 2θ/min, respectively. Typically, x-ray diffraction patterns are acquired within the range of 2θ = 5° to 120°.

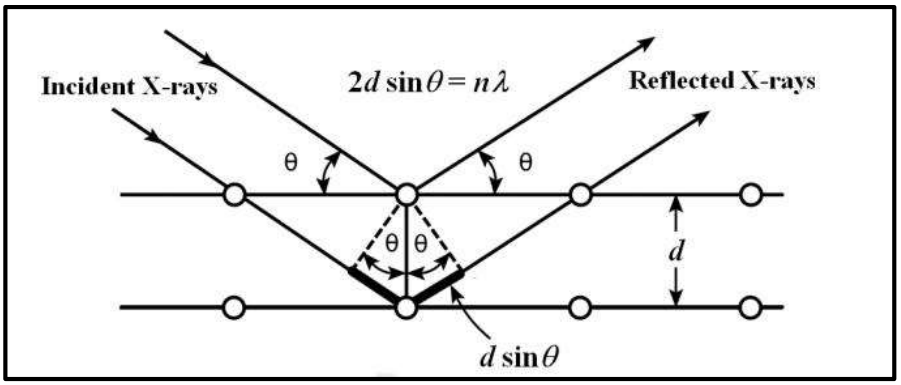

Figure 2.6: schematic diagram illustrating Bragg's law.

The current thesis utilized a Rigaku Miniflex X-ray diffractometer (Cu Kα with λ = 1.54 Å) operating in a Bragg-Brentano configuration to acquire the XRD data. The x-ray diffractometer was equipped with a graphite monochromator, and the x-ray wavelength employed was 1.5418 Å. The XRD data was indexed and matched with Joint Committee on Powder Diffraction Standards data (JCPDS) to confirm the phase purity of the samples.

2.3.2 X-ray Rietveld refinement using Full-proof software

The X-ray diffraction patterns were analyzed using the Rietveld refinement method with the FullProf program [133][134]. This method assesses the phase purity of the samples and provides valuable information about the crystal structure, including lattice parameters, atomic position, occupancy, bond length, bond angle, and many more [135]. It minimizes the difference between the experimental and calculated XRD patterns through a non-linear least square approach. The refinement process involves optimizing the background using a polynomial function and selecting a Pseudo-Voigt function to optimize the peak shape. Various parameters, such as coefficients of the background polynomial, scaling factor,

FWHM parameters (u, v, w), and lattice parameters (a, b, c), were primarily adjusted during the refinement. Additionally, fractional atomic coordinates (x, y, z), isotropic displacement parameters (temperature), and occupancy values were varied. In this context, occupancy refers to the multiplicity of the Wyckoff position divided by the maximum multiplicity of the same space group.

The reliability factors like R_p (profile factor), R_{wp} (weighted profile factor), R_{exp} (expected weight factor), and χ^2 (reduced chi-square) was used to evaluate the quality of Rietveld refinement as follows:

$$R_p = 100 \frac{\sum_{i=1,n} |y_i - y_{c,i}|}{\sum_{i=1,n} y_i} \ldots\ldots (2.1)$$

Here, y_i and y_{ci} denote the experimental and calculated data points, respectively. The total number of data points is given by n.

$$R_{wp} = 100 \left[\frac{\sum_{i=1,n} \omega_i |y_i - y_{c,i}|^2}{\sum_{i=1,n} \omega_i y_i^2} \right]^{1/2} \ldots\ldots (2.2)$$

Here, $\omega_i = {}^{1}/_{\sigma_i^2}$, with σ_i^2 is the variance of the observation y_i.

$$R_{exp} = 100 \left[\frac{n-p}{\sum_{i=1,n} \omega_i y_i^2} \right]^{1/2} \ldots\ldots (2.3)$$

Here n and p represent the total number of experimental points and refined parameters, respectively. The total number of degrees of freedom is given by n-p.

$$\chi^2 = \left[\frac{R_{wp}}{R_{exp}} \right]^2 \ldots\ldots (2.4)$$

The bond lengths/interatomic distances and bond angles were calculated using the optimized fractional coordinates and lattice parameters by using the Vesta program available in the FullProf suite [133].

2.3.3 X-ray photoelectron spectroscopy

X-ray photoelectron spectroscopy (XPS) is a technique used to obtain information about the composition of a surface, the electronic states, and the valence state of elements. In XPS, a beam of X-rays with a specific energy range is directed at the sample. The X-rays are absorbed by the electrons associated with the atoms in the sample, causing some of these electrons, known as photoelectrons, to be ejected from the surface. These photoelectrons have low energy and typically escape to a depth of approximately 10 nm, which is near the surface region of the sample. By measuring the energy of the ejected electrons, it is possible to determine the atomic species present and identify the types of bonds present in the sample. This process follows the law of energy conservation, expressed by the equation:

$$E_K = h\upsilon - E_B \dots\dots (2.5)$$

where h represents Planck's constant, υ is the frequency of the X-ray photon, E_K denotes the kinetic energy of the photoelectron, and E_B represents the electron binding energy of the i^{th} level. An energy spectrum can be generated by determining the number of electrons at different binding energies, which shows an intensity versus binding energy plot. The specific binding energy of an electron serves as a blueprint for identifying the composition of the sample, with the intensity indicating the quantity of the element present. To achieve high-resolution XPS (HR-XPS), an additional monochromator can be incorporated into the XPS system to minimize energy width dispersion. This setup also enables the reduction of spectral background and the elimination of undesired X-rays. Typically, the detection limit for XPS lies within the parts per thousand range, however, increasing the signal collection time can give a higher resolution [136].

2.3.4 Raman Spectroscopy

Raman and FTIR spectroscopy rely on the distinct vibrations of a molecule, allowing for material identification. However, Raman spectroscopy provides additional information about lower frequency vibrations, which can reveal valuable information about the crystal lattice. In Raman spectroscopy, light is scattered to interact with chemical bonds within a substance. When a high-intensity laser illuminates the molecule, most of the scattered light maintains its wavelength as the source, a phenomenon called Rayleigh or elastic scattering. However, some of the scattered radiation experiences energy loss or gain at different

wavelengths, depending on the material's chemical composition or crystallographic nature. This phenomenon is referred to as Raman or inelastic scattering [137]. In the Raman scattering process, the sample absorbs photons from the laser light and re-emits with a shifted frequency. This frequency shift provides valuable information about the rotational, vibrational, and other low-frequency transitions occurring in molecules.

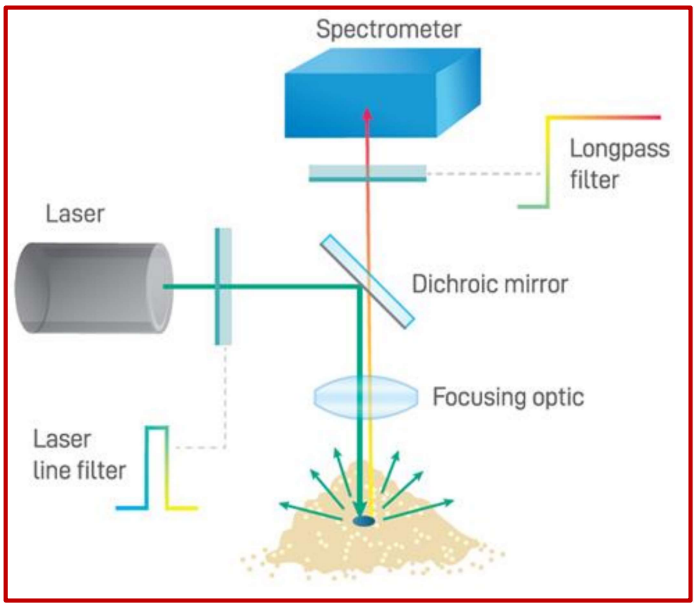

Figure 2.7: Schematic diagram for the simplified setup of Raman spectroscopy.

Figure 2.7 illustrates the experimental setup of Raman spectroscopy, which consists of; a Raman spectrometer, a measurement cell, and a detector. A laser source is utilized to direct the focused beam toward a dichroic filter, which reflects the beam to the sample at a 90° angle. The resulting scattered beam, having the same wavelength, is then directed back to the dichroic filter. Only the Raman scattered beam, with a different wavelength, is able to pass through the filter without any alteration. Mirrors are employed to guide the measured light to a monochromator that employs a grating to diffract the beam and isolate a narrow range of wavelengths. The detector measures the photocurrent corresponding to each specific wavelength. For the present study, Jobin Yvon Horiba's HR 800 and RENISHAW in Via, both Raman spectrometers are used for material identifications.

2.3.5 TGA-DSC

The TGA analysis, is a technique employed to check the thermal durability of materials. This method involves measuring the sample's mass as a function temperature, allowing for mass changes (such as absorption or desorption), phase transitions, and thermal decomposition. When the sample's mass remains constant within a specific temperature range, it denotes thermal stability in that range. TGA analysis also aids in determining the calcination temperature, acting as an upper limit where the sample starts degrading.

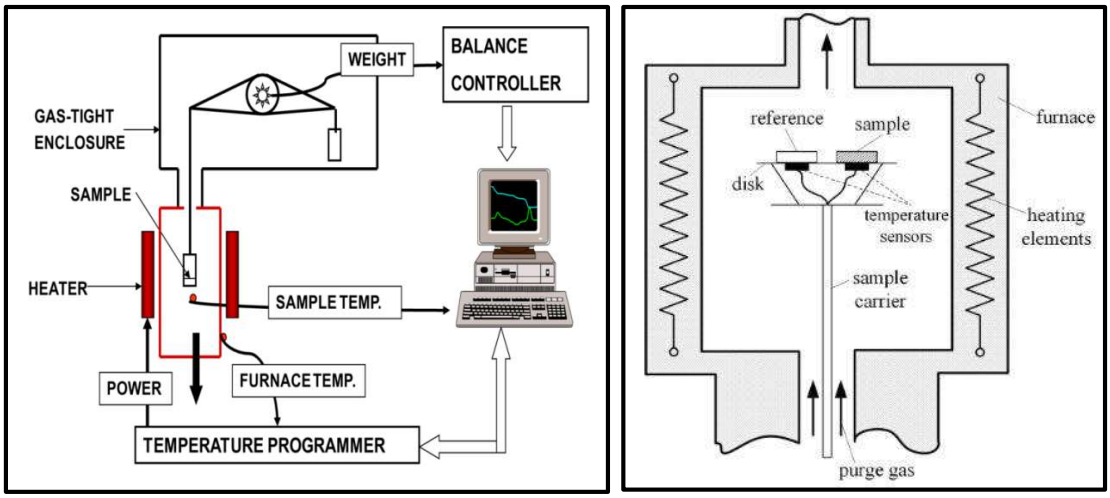

Figure 2.8: A block diagram of TGA-DSC instrument.

Whereas, differential scanning calorimetry (DSC) is a thermal analysis technique used to observe changes in thermal behavior during phase transitions within a system. The difference in the heat required to raise the temperature of the test sample compared to the reference sample is measured, in order to keep both at the same temperature. The sample material is typically placed in a small capsule made of alumina along with an inert powder like α-Al_2O_3, which doesn't exhibit any heat-related effects. The two capsules are heated at a constant rate, and the temperature difference is plotted either against time or against specific temperature points within the apparatus. If any changes occur to the test sample, resulting in either release of heat or absorption of heat, the temperature of the sample will increase or decrease compared to the reference sample. This increase or decrease in temperature indicates either process is an exothermic peak or endothermic. On the other hand, the magnitude of the peaks can be used to quantify the amount of heat released or absorbed during the physical or

chemical changes. In this thesis work, TGA & DSC has been carried out on multiple samples in the temperature range of 30 °C to 800 °C in a nitrogen gas atmosphere [138].

2.3.6 BET (Brunner-Emmett-Teller) surface area measurement

The BET surface area analysis is used to determine the specific surface area and pore size distribution of the materials. The BET technique involves the physical adsorption of nitrogen gas (adsorbate) onto the solid material (adsorbent), which allows us to determine its specific surface area. This physical adsorption relies on the van der Waals force between the gas and the material. After the gas is adsorbed, desorption occurs. The amount of gas adsorbed indicates the specific surface area of the sample. The BET process is typically conducted at a constant temperature, maintained by liquid nitrogen, while the pressure or concentration of the adsorbate gas gradually increases. Therefore, a graph has been plotted between the relative pressure of the gas and the volume adsorbed onto the sample [139][140].

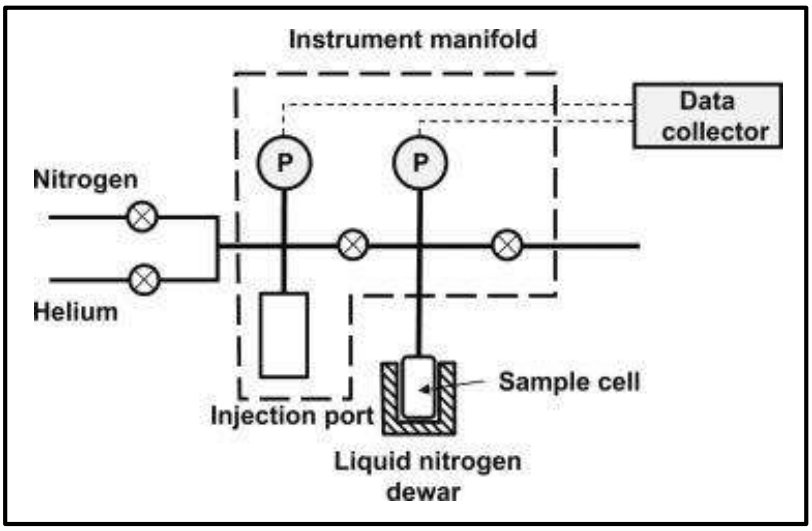

Figure 2.9: Schematic working principle of a BET surface area analyser.

The BET measurement involves three steps:

(i) Standardization of the reference cell.

(ii) The sample undergoes pre-treatment through heating at a specific temperature.

(iii) The adsorbate is adsorbed onto the adsorbent under isotherm conditions.

2.3.7 Transmission electron Microscopy (TEM)

TEM is a powerful instrument, that enables material characterization and offers diverse information through the bright field (BF) and dark field (DF) imaging, selected area diffraction (SAD), and high-resolution lattice imaging. To prepare the samples, a fine-ground powder is mixed with ethanol and subjected to ultrasonication for approximately 50 minutes. Once properly mixed and homogenized, the sample is drop-cast onto a copper grid and dried in an oven overnight at 80 °C. The investigation involves both diffraction and imaging modes. BF and DF imaging are utilized to analyze defects and domain structures, while SAD combined with crystal tilting allows for reconstructing reciprocal space and obtaining crystal structure information and phase identification. In TEM, a high-energy electron beam (~200 keV) passes through the specimen, interacting with it and generating signals that provide information about the internal structure and chemistry of the specimen. Electron diffraction patterns and lattice images are two types of output data that reveal valuable crystallographic information about the material.

Once electrons enter the specimen, they predominantly undergo elastic scattering by the atomic nuclei in the sample. However, there is also a portion of electrons that experience inelastic scattering by the nuclei. This interaction between electrons and the specimen is much more sensitive compared to X-ray or neutron diffraction, resulting in multiple scattering events (Fig. 2.10). Electrons passing close to the nuclei experience some acceleration, leading to a slight decrease in wavelength and a consequent small phase change in the electrons. This phase change carries information about the structure of the specimen. The elastically scattered electrons are the most important in obtaining high-resolution images. The inelastically scattered electrons mainly contribute to the background image. Furthermore, these inelastically scattered electrons generate Kikuchi lines in the electron diffraction pattern, which is helpful in the precise alignment of the crystal within the specimen [141].

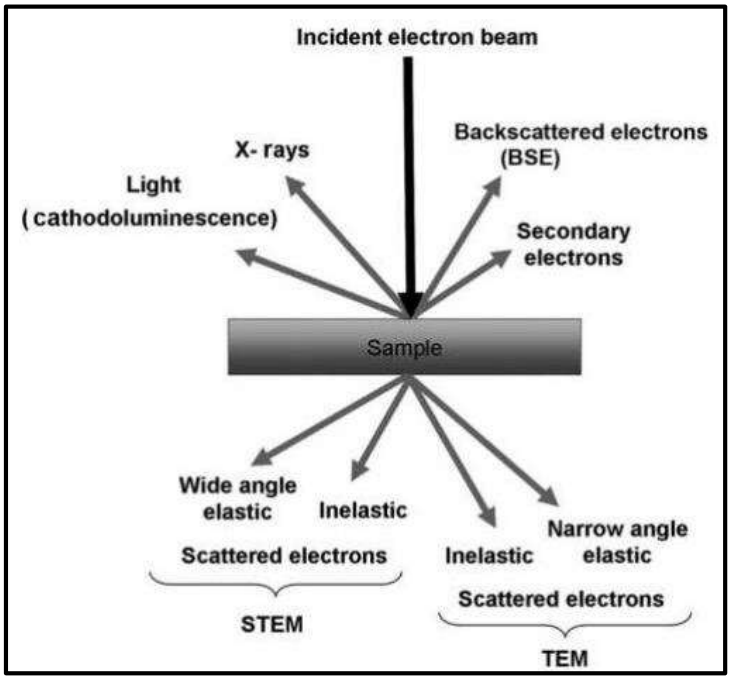

Figure 2.10: Interaction of electrons with sample [141].

2.3.8 Scanning Electron Microscope (SEM)

A scanning electron microscope (SEM) utilizes a focused electron beam to produce images of a sample. In the SEM, a cathode within the electron gun emits a narrow electron beam, both at low and high energy levels. This feature enhances the spatial resolution of the microscope while minimizing potential charging or damage to the sample. The vacuum within the microscope generates the electrons, and the beam passes through electromagnetic lenses, which then focus it onto the specimen. This interaction generates various types of electrons. A detector is used to detect secondary electrons, and by comparing the intensities of secondary and primary electrons, an image of the sample surface is formed. The interaction between the electrons and the atoms in the sample produces different signals that can be detected and provide information about the morphology and composition of the sample. The electron beam scans the sample in a raster pattern, and by combining the beam's position with the detected signal, an image is produced [142][143]. In the present work, the image of the material was taken using the EVO18 microscope manufactured by Zeiss in Japan, as depicted in Fig. 2.11

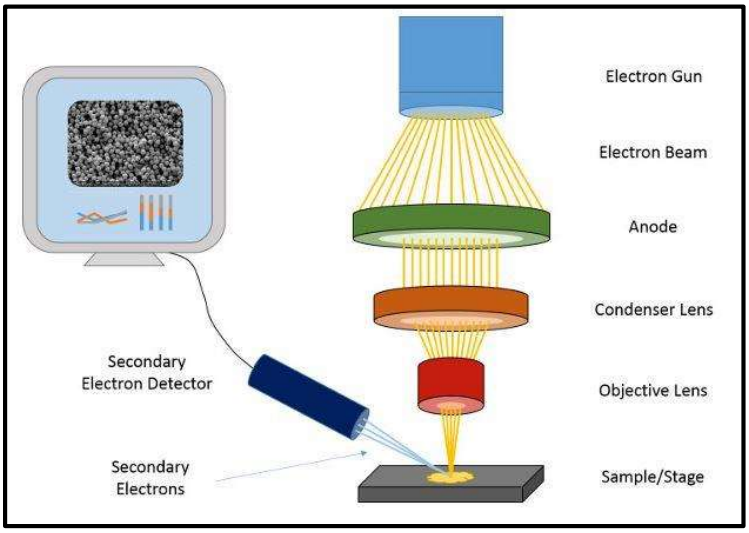

Figure 2.11: Schematic illustration of an SEM.

2.3.9 Energy Dispersive X-Ray Spectroscopy (EDAX)

The Energy Dispersive X-Ray analysis is a non-destructive method used to determine the elemental composition of materials. It is commonly attached to structural analysis techniques like SEM and TEM. These techniques involve a high-energy electron beam that ejects electrons from the inner shell of the atomic orbital to identify the elemental compositions of the specimen. When an electron is removed from the inner shell, the resulting empty space is filled by electrons from nearby shells, which emit X-rays. By analyzing the energy of the emitted X-rays, one can get information about the elements present in the samples. In this thesis, we utilized EDAX in conjunction with SEM and TEM to examine the electron mapping of the composition. Figures. 2.10 and 2.11 illustrate the setup of SEM and TEM connected to the EDAX spectrometer [144].

2.4 Electrochemical Measurements

In order to power the advanced electronics, a potentiostat is required for running electrochemical experiments. Fig. 2.12 represents a block diagram of a commercially available potentiostat (Pine Research) with its equivalent electronic scheme [145]:

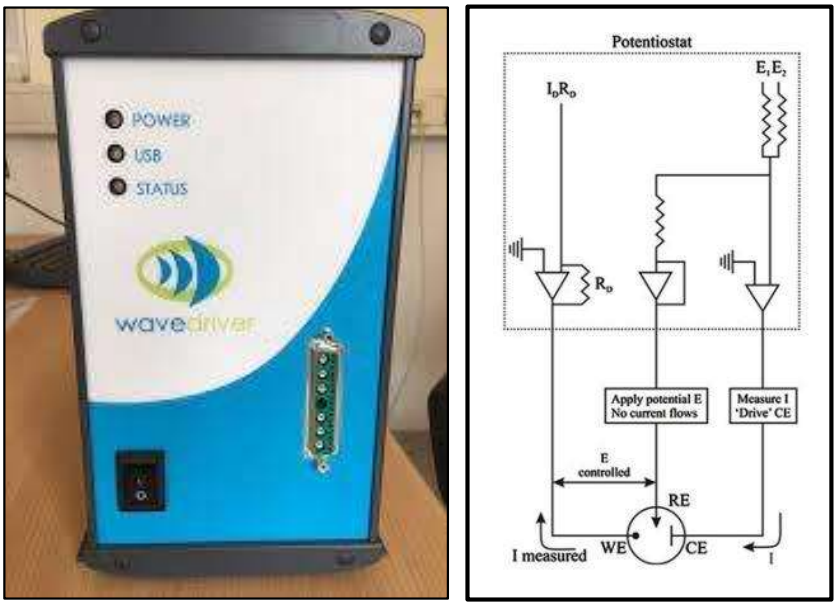

Figure 2.12: Block diagram of a commercially available potentiostat (Pine Research) with its equivalent electronic scheme [145]**.**

There are basically two types of configurations in which different types of electrochemical testing has been performed; three-electrode and two-electrode configurations.

2.4.1 Three-electrode configuration

The three-electrode configuration consists of three electrodes: a working electrode (WE) with the active material, a reference electrode (RE) such as Ag/AgCl or saturated calomel electrode (SCE), and a counter/auxiliary (CE) electrode made of platinum wire. To carry out experiments, these electrodes are immersed in an appropriate electrolyte solution, which can be aqueous or non-aqueous. This type of arrangement is commonly used to investigate the redox behavior of the active material and to examine the chemical processes occurring on the electrode surface, whether they are diffusion or kinetic-controlled processes. However, a huge discrepancy has been observed, while attempting to calculate the capacitance, energy storage, and power delivery efficiency of a device. The diagram below depicts a typical three-electrode configuration used for evaluating the performance of the active materials.

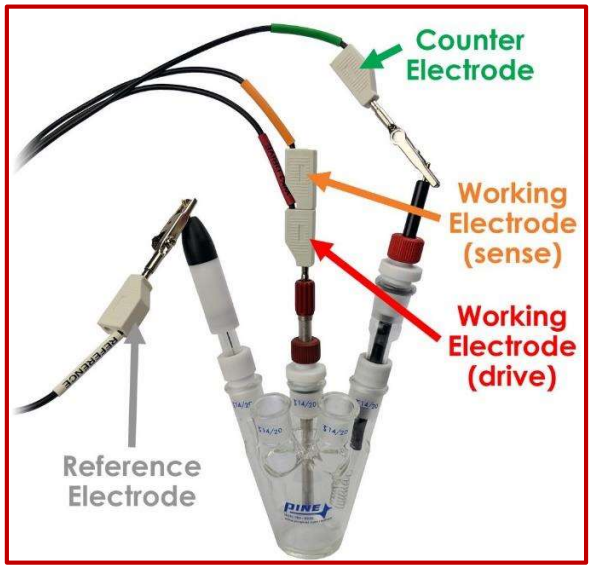

Figure 2.13: Three-electrode arrangement used for the electrochemical measurement

2.4.2 Two-electrode system (full-cell mode)

On the other hand, in a two-electrode setup, two working electrodes are separated by a porous membrane soaked with electrolyte. The working electrode is fabricated by applying active materials onto a current collector, such as carbon fiber paper or various metal foils like nickel, gold, or stainless steel. Typically, reference electrodes are not utilized in this configuration, but they can be induced in some cases to monitor potential changes during charging or discharging. This design closely resembles supercapacitor or battery prototypes and allows exact estimation of capacitance, energy, and power values. Various types of two-electrode test cells, such as Swagelok-type, coin cells, or pouch cells Fig. 2.14, are commercially available [146]. One can make it in the laboratory as per the required dimension.

The measurement techniques used in both two- and three-electrode configurations are nearly identical. However, comparing the results and mathematical calculations obtained from each case may create confusion and misinterpretations, this can lead to the use of proper application of these two configurations. A general electrochemical reaction pathway is depicted in Figure 2.15 [145].

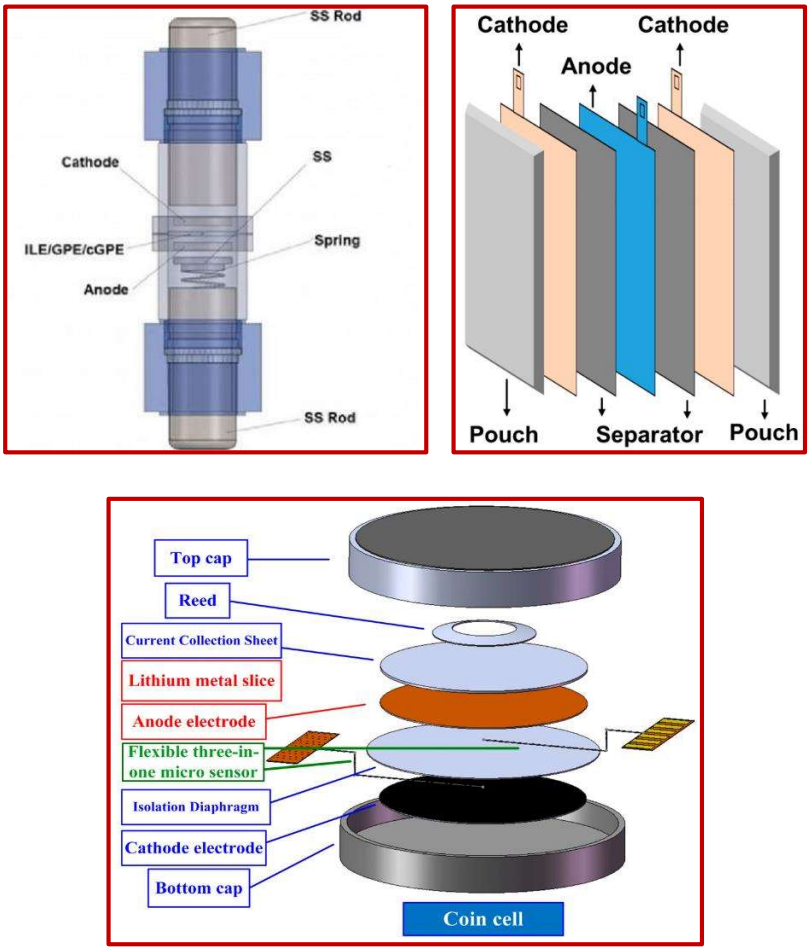

Figure 2.14: various types of two-electrode configurations used for the testing of supercapacitor performances [146].

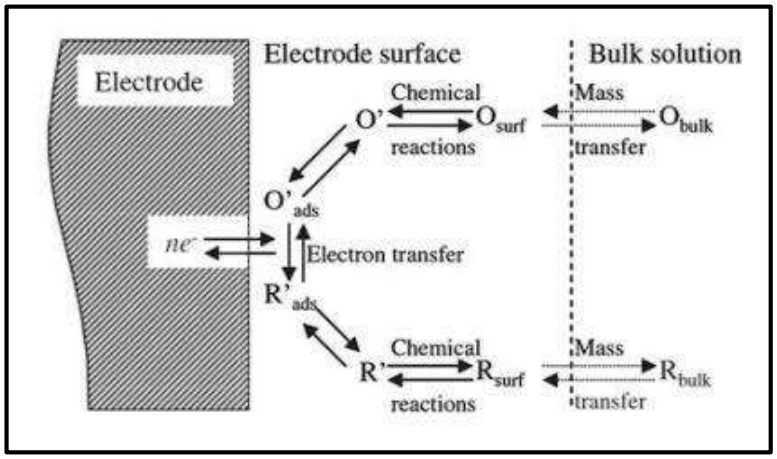

Figure 2.15: A general electrochemical pathway [145].

There are three major experimental techniques used for evaluating the electrochemical performance of a supercapacitor: cyclic voltammetry (CV), galvanostatic charge-discharge (GCD), and electrochemical infrared spectroscopy (EIS).

2.4.3 Cyclic Voltammetry (CV)

Cyclic voltammetry (CV) is a widely employed in analytical chemistry for examining the thermodynamics of redox reactions, kinetics of electron transfer, and detecting the adsorption behavior of substrates on electrodes. In the field of electrochemistry, it is utilized to investigate the behavior of redox reactions, measure the specific capacitance, and talks about the stability of electrode materials. Voltammograms are graphical representations of the relationship between applied potential and current density, derived from continuous potential scanning and measuring the current at the working electrode. Potentiostat will create a potential difference between the working electrode and reference electrode and measure the current response between the working electrode and counter electrode. The working electrode is an electrode over which the reaction of interest occurs and mostly used glassy carbon, graphite sheet, or carbon paper coated with active material. The counter electrode exhibits inert behavior throughout the reaction interval and mostly used platinum or graphite electrodes. Figure 2.16 shows a typical cyclic voltammetry curve for an electrochemical process, which have peak height (Ip) and peak potential (Ep), giving a characteristic feature of a redox reaction [147].

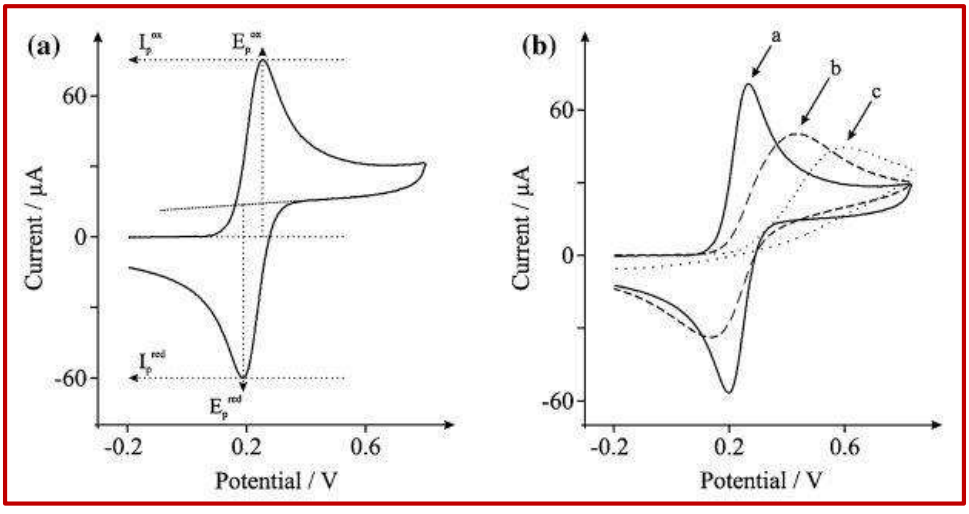

Figure 2.16: (a)Typical cyclic voltammogram depicting the peak position E_P and peak height I_P. (b) CVs for reversible (a), quasi-reversible (b), and irreversible (c) processes.

2.4.4 Galvanostatic Charge-Discharge (GCD)

In this technique, continuous charging and discharging are carried out for three-electrode or two-electrode configurations. During the charging/discharging process, the potential changes over time under a constant applied current. Like the CV technique, the shape of the resulting curve offers valuable insights into the charge storage process, including iR drop, the percentage contribution of double-layer and faradic charge storage, and the effective series resistance of the supercapacitor device. However, applying this method to three-electrode and two-electrode configurations gives distinct outcomes. When current is applied, due to internal resistance the potential of the working electrode changes abruptly, after that it changes gradually due to the development of concentration gradient over-potential developed across the electrode surface [148]. Using the GCD technique, the specific capacitance, resistance, and cyclic performance of the device can be calculated precisely. The voltage equation for GCD is given below:

$$t = iR + \frac{t}{C} i(V) \dots\dots (2.6)$$

From the charge-discharge curve, the specific capacitance of the electrode can be calculated:

$$C_{sp} = \frac{i\Delta t}{m\Delta V} \dots\dots (2.7)$$

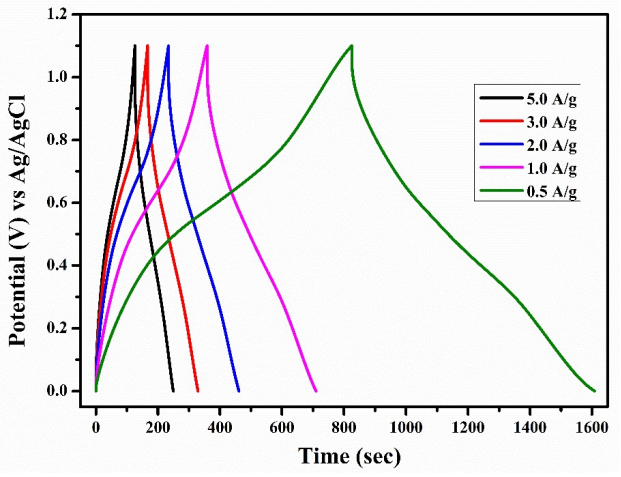

Figure 2.17: represents a typical charge-discharge curve of a supercapacitor.

2.4.5 Electrochemical Impedance Spectroscopy (EIS)

Electrochemical impedance spectroscopy is a method used to examine the frequency response of a supercapacitor device by applying a low-amplitude AC signal to maintain linearity. By employing the EIS technique, the complex impedance and phase angle of the supercapacitor can be assessed across a range of frequencies typically between 0.01 and 1000 Hz. This technique yields two graphical representations known as the Bode plot and Nyquist plot. The former demonstrates the relationship between frequency and phase angle, while the latter displays both the real and imaginary impedance values of the device. The frequency response observed in EIS is directly related to the potential sweep rate employed in cyclic voltammetry. The Bode plot is particularly useful in determining the gain and phase response of the system, capacitive behavior is indicated by a gradual increase in the phase angle up to 90°, while a plateau at a 45° slope may be associated with the pseudocapacitive response of the electrode material [149]. The EIS technique is particularly useful for calculating the effective series resistance (ESR), which provides an accurate calculation of the specific power of a supercapacitor device. By employing the Nyquist plot, various processes taking place at the electrode surface can be analyzed. Generally, the impedance spectra can be divided into three main segments; first, a semicircular region in the high-frequency range represents the charge transfer resistance. second, a linear portion making a slope of 45° with the abscissa called the Warburg element at the mid-frequency (knee frequency) zone, indicating solid-state diffusion, and lastly, a linear portion with a steep slope is observed in the low-frequency region, which corresponds to double-layer capacitance.

2.5 Kinetics of the electrochemical reaction using CV curve

The type of supercapacitor device can be distinguished by Current-Voltage response. This section discusses the kinetics of pseudocapacitance by cyclic voltammetry polarization curve. The electrochemical signature of pseudocapacitance can be described by the following factors:

(i) A linear or pseudo-linear relationship between the applied potential and state of charge (which allows for the calculation of a capacitance, dQ/dV)
(ii) Nearly ideal electrochemical reversibility,
(iii) Surface-controlled kinetics.

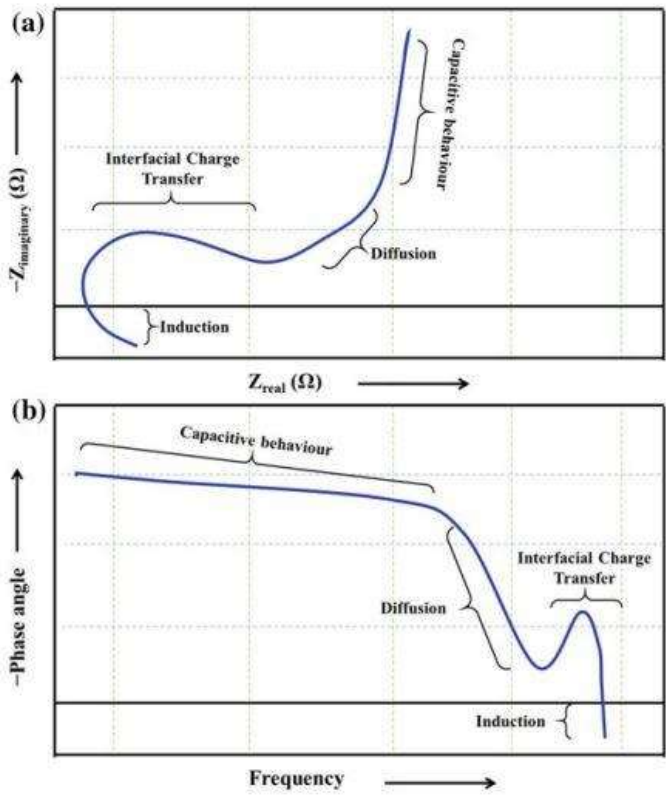

Figure 2.18: (a) Nyquist and (b) Bode plots for both supercapacitors and batteries.

Lindstrom et al. conducted an experiment on the insertion of Li^+ ions into nanoporous anatase TiO_2 films. They established a straightforward correlation between the sweep rate and the observed current. This correlation is known as b-value analysis and is valuable for identifying whether the kinetics are surface-controlled/capacitive or semi-infinite diffusion-controlled [150].

$$i(V) = av^b \dots\dots (2.8)$$

$$\log i(V) = \log a + b \log v \dots\dots (2.9)$$

where, $i(V)$ represents the current at a particular potential, while a and b are adjustable parameters. The value of b can be determined by the slope of log *i* versus log *v* for different sweep rates. The range of the b-value is from 1 to 0.5. A value of b = 1 indicates surface-controlled process, implying a direct relationship between the current and the sweep rate.

There are two potential explanations for this phenomenon. Firstly, the current is influenced by the formation of the EDL:

$$i = C_{dl} A\upsilon \ldots\ldots (2.10)$$

Where, C_{dl} represents the capacitance of the double layer per unit surface area, while A denotes the electrochemically active area of the electrode. Secondly, the current is due to the surface-confined redox processes [151]:

$$i = \frac{nF^2}{4RT} A\Gamma\upsilon \ldots\ldots (2.11)$$

where, n is the number of transferred electrons and Γ is the amount of redox-active adsorbed species at the surface (mol/cm^2). Regardless of whether the mechanism is attributed to double-layer capacitance or surface-confined redox processes, the correlation between current and sweep rate remains constant, characterized by b = 1. Consequently, alternative techniques must be employed to differentiate between these two processes.

When b = 0.5, the reaction follows a semi-infinite diffusion-controlled mechanism, and the current obeys the Randles–Sevcik equation:

$$i = 0.495\, nFAC^* D^{1/2} \left(\frac{\alpha nF}{RT}\right)^{1/2} \upsilon^{1/2} \ldots\ldots (2.12)$$

Where C* is the maximum concentration of the reduced species in the structure and α is the charge transfer coefficient.

Considering mixed assumptions, Liu et al. purposed the following relation [150]:

$$i(V,\upsilon) = K_1(V)\upsilon + K_2(V)\upsilon^{\frac{1}{2}} \ldots\ldots (2.13)$$

Dunn et al. applied this idea to separate capacitive and diffusive components of the overall current in various nanostructured transition metal oxides [152]–[154].

$$\frac{i(V,\upsilon)}{\upsilon^{1/2}} = K_1(V)\upsilon^{\frac{1}{2}} + K_2(V) \ldots\ldots (2.14)$$

By determining the values of K_1 and K_2 under various sweep rates and specific potentials, one can quantify the proportion of current attributed to surface and diffusion-controlled processes. Fig. 2.19 represents cyclic voltammograms of nanostructured anatase TiO_2 films at 0.5 mV/s, demonstrating surface-controlled and diffusion-controlled regions, in a nonaqueous Li^+ electrolyte. However, an important drawback of this method is that it does not account for the shift of potential with higher sweep rates, which is caused by increased ohmic losses [155][156].

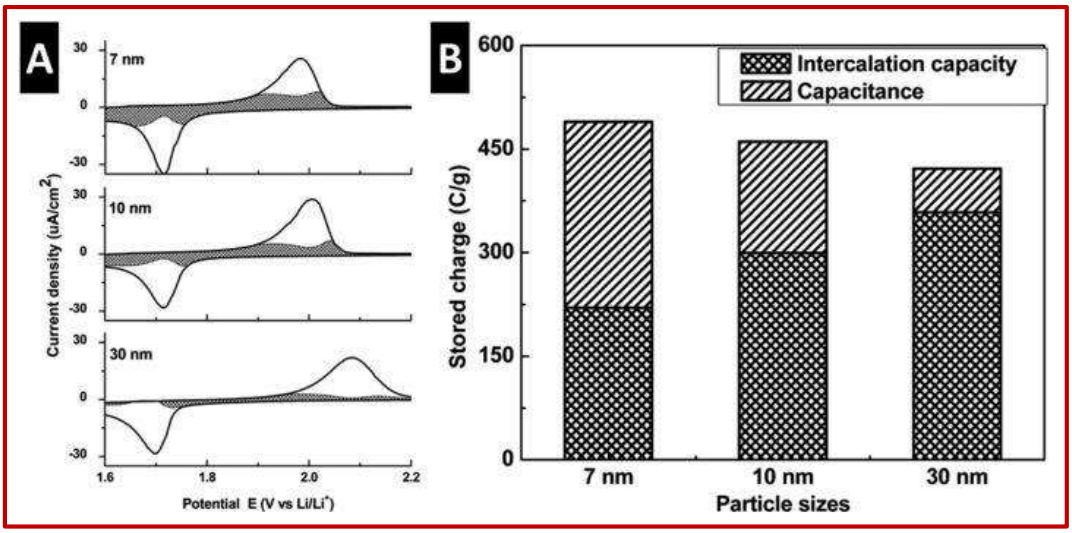

Figure 2.19: (A) CVs of nanostructured anatase TiO_2 films at 0.5 mV/s (B) Charge-storage contribution for different TiO_2 sizes.

Shao et al. developed multiple-step chronoamperometry (MUSCA) as a solution to minimize the impact of the ohmic drop. MUSCA was based on the potentiostatic intermittent titration technique (PITT) [155]. In PITT, each potential step is maintained until equilibrium is reached, and the current is recorded at short intervals similar to chronoamperometry. Fig. 2.20A illustrates a typical potential waveform and its corresponding current response [156]. MUSCA was applied to reconstruct voltammograms for $Ti_3C_2T_x$ MXene in aqueous 3 M H_2SO_4, resulting in less peak shifts compared to those obtained from cyclic voltammetry (Fig. 2.20 B and C). By utilizing the reconstructed voltammograms, the analysis of K_1 and K_2 can be used to separate surface and diffusion-controlled contributions to the current at different potentials.

Donne et al. employed the voltammogram reconstruction technique to develop step potential electrochemical spectroscopy (SPECS) [157]–[159]. This method is designed to deconvolute electrochemical mechanisms by fitting the current response ($i_{overall}$) with a combination of capacitive (i_C), diffusion-controlled (i_D), and residual (i_R) currents:

$$i_{overall} = i_C + i_D + i_R \dots\dots (2.15)$$

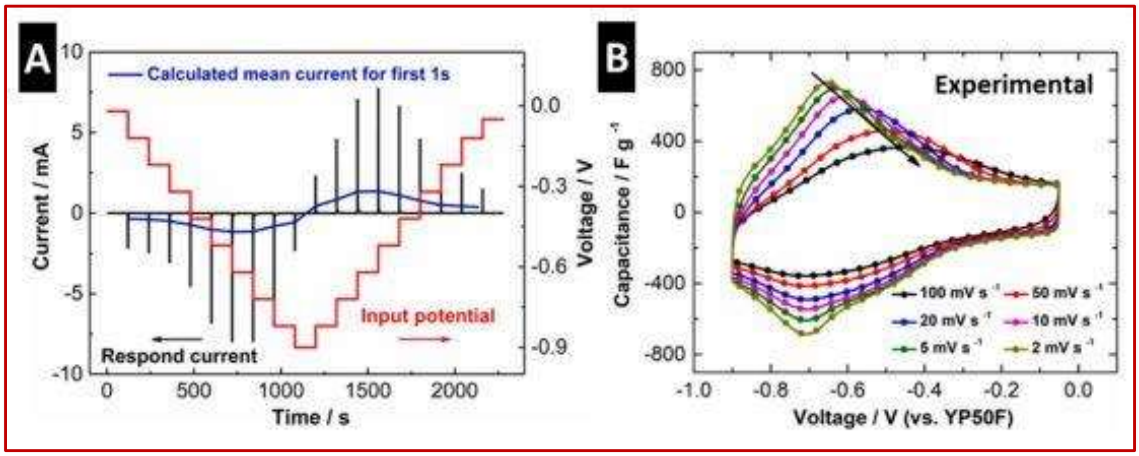

Figure 2.20: (A) The potential waveform and current response of a$Ti_3C_2T_x$ MXene electrode in aqueous 3 M H_2SO_4. (B) Experimental cyclic voltammograms and (C) reconstructed cyclic voltammograms at sweep rates from 2 to 100 mV/s.

Trasatti et al. developed a method that utilizes voltammetric charge to separate the contributions of the "inner" (less accessible) and "outer" (more accessible) surfaces [160]. The

method assumes that the voltammetric charge (Q) can be divided into surface-controlled and diffusion-controlled components such that

$$Q = Q_s + Q_d \dots\dots (2.15)$$

where Q_s and Q_d are the surface-controlled and diffusion-controlled contributions to charge, respectively. The surface-controlled component can be further divided into the "inner" surface contribution, $Q_{s,in}$ and "outer" surface contribution, $Q_{s,out}$:

$$Q_s = Q_{s,in} + Q_{s,out} \dots\dots (2.16)$$

The impact of the "inner" surface is influenced by the sweep rate due to the low accessibility of redox sites, while the impact of the "outer" surface remains constant regardless of the sweep rate. Hence,

$$Q_s = f(x) = \begin{cases} Q_{s,out} & when\ \upsilon = \infty \\ Q_{s,in} + Q_{s,out} & when\ \upsilon = 0 \end{cases} \dots\dots (2.17)$$

By imposing these conditions, it is possible to estimate the values of $Q_{s,out}$ and $Q_{s,in}$ by extrapolating the charge against the sweep rate. Assuming a semi-infinite diffusion and a linear relationship between Q_d and $\nu^{-1/2}$, it can be rearranged to ascertain $Q_{s,out}$ when $\nu=\infty$:

$$Q = Q_{s,out} + A_1 \upsilon^{-1/2} \dots\dots (2.18)$$

where A_1 is a constant. In a plot of Q vs $\nu^{-1/2}$, the y-intercept ($\nu^{-1/2} = 0$; or $\nu = \infty$) determines $Q_{s,out}$. On the other hand, $Q_{s,in}$ is determined when $\nu = 0$. Assuming Q^{-1} decreases linearly with $\nu^{1/2}$, and can be rewritten as

$$Q^{-1} = Q_s^{-1} + A_2 \upsilon^{1/2} \dots\dots (2.19)$$

where A_2 is another constant. Q_s^{-1} can be obtained from the y-intercept ($\nu^{1/2} = 0$) in a plot of Q^{-1} vs $\nu^{1/2}$. $Q_{s,in}$ can be obtained.

The Trasatti method, like the K_1, K_2 analysis, does not account for ohmic losses and irreversible side reactions. However, it is considered applicable within a specific reliability range, thereby reducing the impact of interfering factors [161].